

Observation of universal strong orbital-dependent correlation effects in iron chalcogenides

M. Yi^{1,2†}, Z.-K. Liu^{1,2†}, Y. Zhang^{1,3†}, R. Yu^{4,5}, J.-X. Zhu⁶, J. J. Lee^{1,2}, R. G. Moore¹, F. T. Schmitt¹, W. Li¹, S. C. Riggs^{1,2}, J.-H. Chu⁷, B. Lv⁸, J. Hu⁹, M. Hashimoto¹⁰, S.-K. Mo³, Z. Hussain³, Z. Q. Mao⁹, C. W. Chu⁸, I. R. Fisher^{1,2}, Q. Si⁵, Z.-X. Shen^{1,2*}, and D. H. Lu^{10*}

¹*Stanford Institute for Materials and Energy Sciences, SLAC National Accelerator Laboratory and Stanford University, Menlo Park, California 94025, USA*

²*Departments of Physics and Applied Physics, and Geballe Laboratory for Advanced Materials, Stanford University, Stanford, California 94305, USA*

³*Advanced Light Source, Lawrence Berkeley National Lab, Berkeley, California 94720, USA*

⁴*Department of Physics, Renmin University of China, Beijing 100872, China*

⁵*Department of Physics and Astronomy, Rice University, Houston, Texas 77005, USA*

⁶*Theoretical Division, Los Alamos National Laboratory, Los Alamos, New Mexico 87545, USA*

⁷*Department of Physics, University of California, Berkeley, California 94720, USA*

⁸*Department of Physics, Texas Center for Superconductivity, University of Houston, Houston, Texas 77204, USA*

⁹*Department of Physics and Engineering Physics, Tulane University, New Orleans, Louisiana 70118, USA*

¹⁰*Stanford Synchrotron Radiation Lightsource, SLAC National Accelerator Laboratory, Menlo Park, California 94025, USA*

[†]*These authors contributed equally.*

**To whom correspondence should be addressed: dhlu@slac.stanford.edu and zxshen@stanford.edu*

Establishing the appropriate theoretical framework for unconventional superconductivity in the iron-based materials requires correct understanding of both the electron correlation strength and the role of Fermi surfaces. This fundamental issue becomes especially relevant with the discovery of the iron chalcogenide (FeCh) superconductors¹⁻³, the only iron-based family in proximity to an insulating phase⁴. Here, we use angle-resolved photoemission spectroscopy (ARPES) to measure three representative FeCh superconductors, $\text{FeTe}_{0.56}\text{Se}_{0.44}$, $\text{K}_{0.76}\text{Fe}_{1.72}\text{Se}_2$, and monolayer FeSe film grown on SrTiO_3 . We show that, these FeChs are all in a strongly correlated regime at low temperatures, with an orbital-selective strong renormalization in the d_{xy} bands despite having drastically different Fermi-surface topologies. Furthermore, raising temperature brings all three compounds from a metallic superconducting state to a phase where the d_{xy} orbital loses all spectral weight while other orbitals remain itinerant. These observations establish that FeChs display universal orbital-selective strong correlation behaviors that are insensitive to the Fermi surface topology, and are close to an orbital-selective Mott phase (OSMP), hence placing strong constraints for theoretical understanding of iron-based superconductors.

Since the discovery of high temperature superconductivity in the iron pnictides (FePn), extensive research efforts have revealed many common properties of these materials. In the vast material base of the FePns, all parents phases are metallic, and the observed electronic structures are largely consistent with the prediction of *ab initio* LDA calculations⁵⁻⁶. These properties have led to theoretical understanding that the electron correlation in FePns is much weaker than in cuprate superconductors, whose parent phases are Mott insulators. Furthermore, the observation of comparable sized hole pockets at the Brillouin zone (BZ) center and electron pockets at the BZ corner have resulted in the proposal that such a FS topology is ubiquitous and essential to

superconductivity in iron pnictides, and pairing in the iron pnictides is mediated by antiferromagnetic fluctuations via Fermi surface nesting between the hole and electron Fermi pockets⁷. On the other hand, there have also been theoretical proposals of ‘incipient Mott localization’ for which the system is metallic but on the verge of localization⁸⁻¹⁰, supported by the normal state bad metal behavior from optical conductivity measurements¹¹ and the large fluctuating magnetic moment comparable to the antiferromagnetic insulating copper oxides¹². This discussion became especially relevant with the more recent discovery of FeChs, which not only possess large local magnetic moments¹³ and insulating phases⁴, but also include compounds that lack hole pockets needed for Fermi surface nesting yet have comparable T_C ’s as FePns¹⁴⁻¹⁷.

To provide insight on the more appropriate theoretical model, we study and compare the three representative superconducting FeChs: $\text{FeTe}_{0.56}\text{Se}_{0.44}$ (FTS), $\text{K}_{0.76}\text{Fe}_{1.72}\text{Se}_2$ (KFS), and monolayer FeSe film grown on SrTiO_3 (FS/STO). FTS, with a T_C of 14.5K, is the optimally substituted member of the $\text{FeTe}_{1-x}\text{Se}_x$ family, in which superconductivity is achieved with isovalent substitution of Se for Te that suppresses magnetic order in the FeTe end¹⁸. KFS, with a T_C of 32K, belongs to the $\text{K}_x\text{Fe}_{2-y}\text{Se}_2$ family, which has in its phase diagram insulating phases with magnetic moments as large as $3.3\mu_B/\text{Fe}$ ^{2,4,13}. FS/STO is the latest addition to the FeCh family with a record T_C possibly exceeding 65K^{3,16-17}. In a previous ARPES study¹⁹ on KFS, we found the low temperature state to be a metallic state with orbital-dependent renormalization—where the d_{xy} orbital dominated bands are strongly renormalized as compared to other orbitals. Raising temperature drives the material to an OSMP in which the d_{xy} orbital completely loses spectral weight while other orbitals remain itinerant. Subsequently, such a temperature scale was also identified by THz spectroscopy²⁰, Hall measurements²¹ and pump-probe spectroscopy²². This motivates the usage of orbital selectivity to address the fundamental open question of

whether it is the electron correlation strength or the nature of the Fermi surface that plays a predominant role in the microscopic physics of the FeCh materials.

The generic electronic structure of iron-based superconductors (FeSC) consists of three hole bands at the BZ center, Γ , and two electron bands at the BZ corner, M. The hole bands are predominantly of d_{xz} , d_{yz} , and d_{xy} orbital characters, while the electron bands are d_{xz} and d_{xy} along Γ -M. The measured band structure along the Γ -M high symmetry direction for the three compounds are shown in Fig. 1e-g, in comparison to that for the optimally Co-doped BaFe_2As_2 (BFCA) (Fig. 1h), an iron pnictide as a reference. For FTS (Fig. 1i), one of the hole bands crosses the Fermi level, E_F , and both electron bands cross E_F at M, resulting in roughly compensated hole pocket at Γ and electron pockets at M (Fig. 1a), consistent with isovalent substitution for this compound. For both KFS (Fig. 1j) and FS/STO (Fig. 1k), in contrast, only the electron bands cross E_F while the hole band tops are well below E_F , signaling heavy electron doping in both compounds as reflected in a Fermi surface topology consisting only of electron pockets at M (Fig. 1b-c). Comparing the band structure of the three FeChs to the FePns, we notice a significant difference near the M point—there is an apparent gap between the bottom of the electron bands and the top of the hole band in all three FeChs, in sharp contrast to BFCA (Fig. 1l), in which the d_{xz} electron band bottom is degenerate with the d_{yz} hole band top.

Generally in FeSC, this degeneracy between the d_{xz} electron band bottom and d_{yz} hole band top at the zone corner is protected by the C_4 rotational symmetry, as seen in BFCA (Fig. 1l) and corresponding LDA calculations (Fig. 1m). This degeneracy is only lifted with the breaking of C_4 symmetry, as in the orthorhombic phase of underdoped BFCA²³. However, no C_4 symmetry breaking has been reported for any of these FeChs, nor are twinning effects observed here that is expected from a broken symmetry due to orthorhombic distortion²³. Rather, this

apparent gap can be explained by a strong orbital-dependent band renormalization. As the schematic shown in Fig. 1m-o, the LDA calculated d_{xy} electron band bottom is deeper than that of the d_{xz} band. If the d_{xy} orbital is strongly renormalized compared to the other orbitals, the d_{xy} electron band bottom, i.e., the corresponding d_{xy} hole band top, would rise above that of the d_{xz} electron band (Fig. 1n). The heavily renormalized d_{xy} hole band then crosses the d_{xz} electron band and the two bands hybridize such that a gap appears at the M point without lifting the d_{xz}/d_{yz} degeneracy protected by C_4 symmetry (Fig. 1o). Evidence for two nearly degenerate electron bands can be seen in the high resolution spectra acquired on FS/STO (Fig. 1p).

This interpretation is further supported by the observed strong renormalization of the d_{xy} hole band near Γ , which is significantly more renormalized than the d_{xz}/d_{yz} hole bands, clearly seen in all three compounds (Fig. 1i-k). For FTS, the d_{xy} hole band is strongly renormalized by a factor of ~ 16 compared to LDA calculations, while d_{xz} and d_{yz} bands are only renormalized by factors of ~ 4 . Moreover, in the $\text{FeTe}_{1-x}\text{Se}_x$ family, it has been found that the d_{xy} band renormalization factor strongly increases towards the FeTe end compared to that of d_{xz}/d_{yz} , further revealing the strong orbital-dependence in the itinerant to localized crossover in this system²⁴. For KFS, the d_{xy} hole band is renormalized by a factor of ~ 10 compared to the factor of ~ 3 for d_{xz}/d_{yz} bands¹⁹. This is even more apparent in FS/STO, where enhanced d_{xy} orbital matrix elements in the second BZ shows the nearly flat d_{xy} hole band extending towards the bottom of the shallow electron bands at M with a noticeable hybridization gap (Fig. 1q). In contrast, in BFCA, the renormalization factor for d_{xy} hole band is comparable to that of the d_{xz}/d_{yz} hole bands ($2\sim 3$)⁶, as can be seen in the band curvatures (Fig. 1l). In summary, all three FeCh systems show much stronger renormalization in the d_{xy} orbital compared to the d_{xz}/d_{yz} orbitals in the low temperature state, in contrast to the FePns.

Next, by raising temperature sufficiently high, we notice that in all three FeCh systems, the d_{xy} orbital-dominated bands lose spectral weight completely (Fig. 2), as reported previously for KFS¹⁹. This can be seen first in the disappearance of the shallow d_{xy} hole band near the Γ point. In the low temperature state of FTS, the d_{xy} hole band crosses the d_{yz} hole band near Γ , and a small hybridization gap appears as can be seen in the discontinuous intensity pattern of the strong d_{yz} hole band (Fig. 2a). At high temperature, this discontinuity disappears as only the d_{xz} and d_{yz} hole bands remain (Fig. 2d). In KFS and FS/STO, the nearly flat d_{xy} hole band in the low temperature state is entirely above the d_{xz}/d_{yz} hole band tops (Fig. 2b), and clearly disappears at high temperatures (Fig. 2e). The second evidence for the disappearance of d_{xy} orbital at high temperatures is the vanishing of the apparent gap between the electron band bottom and the d_{yz} hole band top at M. As shown in the schematic (Fig. 2g-h), when the d_{xy} band disappears, its hybridization gap with the d_{xz} electron band naturally vanishes, recovering the deeper non-hybridized d_{xz} electron band whose bottom is degenerate with the d_{yz} hole band top as expected. This is clearly seen in the high temperature data in all three systems (Fig. 2d-f). Here we note that while KFS is known to have phase separation issues with the existence of superconducting regions and insulating regions¹⁹, FTS and FS/STO, on the other hand, do not have such complication. Hence the universal behavior of vanishing d_{xy} spectral weight with raised temperature observed here reflects an intrinsic effect rather than a result of intricate phase separation in KFS.

To examine this temperature dependence more carefully, we have quantitatively analyzed the spectral weight of each FeCh system. For FTS, we track the d_{xy} hole band slightly away from the Γ point where it is well separated from the d_{yz} hole band (Fig. 3a). From the energy distribution curve (EDC) at this momentum, we fit Gaussian peaks for both d_{xy} hole band near E_F

and d_{yz} hole band at higher energies, along with a Shirley background (Fig. 3d), and track the integrated spectral weight of the d_{xy} and d_{yz} peaks as a function of temperature. Comparing these two orbitals, we see that the d_{xy} spectral weight drops to zero around 110K, in contrast to a very weak decrease of the d_{yz} spectral weight. This is very similar to the situation in KFS and FS/STO, where we track the spectral weight of the d_{xy} orbital at the d_{xy} electron band bottom at M. For KFS, the fitted peak area precipitously drops around 100K, and approaches zero above 180K (Fig. 3h). For FS/STO, the d_{xy} spectral weight approaches zero above 150K while that of the d_{yz} orbital remains finite (Fig. 3i), demonstrating the orbital-dependence of this temperature evolution.

For all three FeCh superconductors studied, two observations are universal: i) strong orbital-dependent renormalization at low temperatures, ii) disappearance of d_{xy} spectral weight with raised temperatures. Theoretically, these behaviors can be understood in proximity to an OSMP, as predicted by both a slave-spin mean-field method²⁵ and dynamical mean field theory method²⁶ taking into account sufficiently strong intra-orbital Coulomb repulsion U and Hund's coupling J . These work show that the FeChs are close to an OSMP in which the d_{xy} orbital is completely Mott localized while the other orbitals remain itinerant. For the first approach, a system sufficiently close to such a phase at low temperatures can crossover into the OSMP via raising temperature due to the larger entropy of the OSMP. For the second approach, an orbital-dependent coherent-incoherent crossover can be induced by raising temperature, where the coherence temperature is the lowest for the d_{xy} orbital such that it would gradually lose coherence with increasing temperature before other orbitals.

The orbital-selectivity initially arises from the crystal field splitting of the tetragonal lattice, where the d_{xy} orbital energy level becomes higher than that of d_{xz}/d_{yz} . Hund's coupling

further suppresses inter-orbital coupling. The degeneracy of the d_{xz}/d_{yz} orbitals allows stronger orbital fluctuations between these two orbitals than with d_{xy} . Hence, the d_{xy} orbital can become Mott localized before that of d_{xz}/d_{yz} , leading to an OSMP. When the material is sufficiently close to such an OSMP, the d_{xy} mass renormalization is much stronger than that of other orbitals, as observed in the low temperature state of the FeChs. For the system to be close to this OSMP, it must exhibit strong electron correlations, which from the two theoretical studies is shown to be a combined result of Coulomb interactions U and Hund's coupling J .

Among the three FeChs, FTS is stoichiometric, with $n=6$, while FS/STO and KFS are electron doped, with $n=6.12$ and 6.15 , as estimated from Fermi surface volume counting. Fig. 4 shows our calculated temperature versus U phase diagrams for systematic dopings from $n=6$ to 6.15 . The blue shading indicates the d_{xy} quasiparticle spectral weight, Z_{xy} , for each doping. When Z_{xy} drops to zero, the system enters the OSMP. Furthermore, we see that for and only for integer filling, $n=6$, there exists a Mott Insulator (MI) phase, where all orbitals become Mott localized with sufficiently large U . With increasing electron filling, the critical U for the system entering the OSMP at a given temperature shifts to larger value, or that electron doping brings the system away from the OSMP. This is consistent with the observation that the temperature at which the d_{xy} spectral weight disappears increases from FTS (110K) to the doped FS/STO (150K) and KFS (180K). Here we note that the resistivity for the $\text{FeTe}_{1-x}\text{Se}_x$ family exhibits a weak hump¹⁸ suggestive of a crossover from insulating-like to metallic-like behavior much like the case of KFS^2 , and this crossover temperature scale shifts to lower value with decreasing x , consistent with the stronger renormalization values towards the FeTe end²⁴ and the understanding that the low temperature state of FeTe end sits closer to the OSMP.

The strong orbital-selective behavior in the FeCh family is a manifestation of its strong electron correlations, and suggests that they may serve as a bridge between the strongly correlated cuprates as doped Mott insulators and the weaker correlated FePns that are more itinerant. As suggested in a recent theoretical work, the strong Hund's coupling in the selective Mott regime suppresses interorbital coupling and could effectively decouple the orbitals into a collection of doped single-band Mott insulators²⁷. This is relevant to the current discussion on the pairing mechanism of FeSC in both KFS and FS/STO as the lack of hole pockets do not seem to prevent them from superconducting at temperatures comparable to or even higher than FePns, which is unexpected from a weak-coupling Fermi surface nesting picture⁷. In a recent theoretical study²⁸, it has been shown that under a strong-coupling approach, where the driving force for pairing comes from the close-neighbor exchange interactions, the pairing strength can be comparable in the FeChs and FePns, as they approach a Mott transition by increasing exchange interaction in the former and reducing the renormalized bandwidth in the latter. The observed universal strong correlation in the FeChs and proximity to an OSMP here supports such a scenario.

Methods

High quality single crystals of $\text{K}_{0.76}\text{Fe}_{1.72}\text{Se}_2$ and $\text{FeTe}_{0.56}\text{Se}_{0.44}$ were grown using the flux method^{19,29}. Monolayer FeSe films were grown on SrTiO_3 using molecular beam epitaxy¹⁷. ARPES measurements were carried out at beamline 5-4 of the Stanford Synchrotron Radiation Lightsource and beamline 10.0.1 of the Advanced Light Source using SCIENTA R4000 electron analyzers. The total energy resolution was set to 10 meV and the angular resolution was 0.3° .

Single crystals were cleaved in situ at 10 K for each measurement. The FeSe films were transported to the beamline under vacuum and further annealed before measurements. All measurements were done in ultra high vacuum with a base pressure lower than 4×10^{-11} torr. The theoretical calculations were done using a slave-spin mean-field method on a five-orbital Hubbard model²⁵, with tight-binding parameters for FTS. Hund's J is fixed at 0.6eV.

References

1. Hsu, F.-C. *et al.*, Superconductivity in the PbO-type structure α -FeSe. *Proc. Natl. Acad. Sci.* **105**, 38 (2008).
2. Guo, J. *et al.* Superconductivity in the iron selenide $K_x\text{Fe}_2\text{Se}_2$ ($0 \leq x \leq 1.0$). *Phys. Rev. B* **82**, 180520(R) (2010).
3. Wang, Q. Y. *et al.* Interface induced high temperature superconductivity in single unit-cell FeSe films on SrTiO₃. *Chin. Phys. Lett.* **29**, 037402 (2012).
4. Fang, M.-H. *et al.* Fe-based superconductivity with $T_C=31\text{K}$ bordering an antiferromagnetic insulator in $(\text{Ti,K})\text{Fe}_x\text{Se}_2$. *Europhys. Lett.* **94**, 27009 (2011).
5. Lu, D. H. *et al.*, Electronic structure of the iron-based superconductor LaOFeP. *Nature* **455**, 81 (2008).
6. Yi, M. *et al.*, Electronic structure of the BaFe_2As_2 family of iron-pnictide superconductors. *Phys. Rev. B* **80**, 024515 (2009).
7. Mazin, I. I., Singh, D. J., Johannes, M. D., and Du, M. H. Unconventional Superconductivity with a Sign Reversal in the Order Parameter of $\text{LaFeAsO}_{1-x}\text{F}_x$. *Phys. Rev. Lett.* **101**, 057003 (2008).

8. Yin, Z. P., Haule, K., and Kotliar, G. Kinetic frustration and the nature of the magnetic and paramagnetic states in iron pnictides and iron chalcogenides. *Nat. Mat.* **10**, 932 (2011).
9. Si, Q. And Abrahams, E. Strong Correlations and Magnetic Frustration in the High T_C Iron Pnictides. *Phys. Rev. Lett.* **101**, 076401 (2008).
10. Yu, R., Zhu, J.-X., and Si, Q. Mott Transition in Modulated Lattices and Parent Insulator of $(K,Tl)_yFe_xSe_2$ Superconductors. *Phys. Rev. Lett.* **106**, 186401 (2011).
11. Qazilbash, M. M. *et al.* Electronic correlations in the iron pnictides. *Nat. Phys.* **5**, 647-650 (2009).
12. Liu, M. *et al.* Nature of magnetic excitations in superconducting $BaFe_{1.9}Ni_{0.1}As_2$. *Nat. Phys.* **8**, 376-381 (2012).
13. Bao, W. *et al.* A Novel Large Moment Antiferromagnetic Order in $K_{0.8}Fe_{1.6}Se_2$ Superconductor. *Chin. Phys. Lett.* **28**, 086104 (2011).
14. Zhang, Y. *et al.* Nodeless superconducting gap in $A_xFe_2Se_2$ ($A=K,Cs$) revealed by angle-resolved photoemission spectroscopy. *Nat. Mat.* **10**, 273 (2011).
15. Qian, T. *et al.* Absence of a Holelike Fermi Surface for the Iron-Based $K_{0.8}Fe_{1.7}Se_2$ Superconductor Revealed by Angle-Resolved Photoemission Spectroscopy. *Phys. Rev. Lett.* **106**, 187001 (2011).
16. Liu, D. *et al.* Electronic origin of high-temperature superconductivity in single-layer FeSe superconductor. *Nat. Comm.* **3**, 931 (2012).
17. Lee, J. J. *et al.* Evidence for pairing enhancement in single unit cell FeSe on $SrTiO_3$ due to cross-interfacial electron-phonon coupling. arXiv:1312.2633.

18. Liu, T. J. *et al.* From $(\pi,0)$ magnetic order to superconductivity with (π,π) magnetic resonance in $\text{Fe}_{1.02}\text{Te}_{1-x}\text{Se}_x$. *Nat. Mat.* **9**, 716 (2010).
19. Yi, M. *et al.* Observation of Temperature-Induced Crossover to an Orbital-Selective Mott Phase in $\text{A}_x\text{Fe}_{2-y}\text{Se}_2$ (A=K,Rb) Superconductors. *Phys. Rev. Lett.* **110**, 067003 (2013).
20. Wang, Z. *et al.* Orbital-selective metal-insulator transition and gap formation above T_C in superconducting $\text{Rb}_{1-x}\text{Fe}_{2-y}\text{Se}_2$. *Nat. Comm.* **5**, 3202 (2014).
21. Ding, X. *et al.* Strong and nonmonotonic temperature dependence of Hall coefficient in superconducting $\text{K}_x\text{Fe}_{2-y}\text{Se}_2$ single crystals. *Phys. Rev. B* **89**, 224515 (2014).
22. Li, W. *et al.* Mott behavior in $\text{K}_x\text{Fe}_{2-y}\text{Se}_2$ superconductors studied by pump-probe spectroscopy. *Phys. Rev. B* **89**, 134515 (2014).
23. Yi, M. *et al.* Symmetry-breaking orbital anisotropy observed for detwinned $\text{Ba}(\text{Fe}_{1-x}\text{Co}_x)_2\text{As}_2$ above the spin density wave transition. *Proc. Natl. Acad. Sci.* **108**, 6878 (2011).
24. Liu, Z. K. *et al.* Experimental Observation of Incoherent-Coherent Crossover and Orbital Dependent Band Renormalization in Iron Chalcogenide Superconductors. In preparations.
25. Yu, R. and Si, Q. Orbital-Selective Mott Phase in Multiorbital Models for Alkaline Iron Selenides $\text{K}_{1-x}\text{Fe}_{2-y}\text{Se}_2$. *Phys. Rev. Lett.* **110**, 146402 (2013).
26. Yin, Z. P., Haule, K., and Kotliar, G. Fractional power-law behavior and its origin in iron-chalcogenide and ruthenate superconductors: Insights from first-principles calculations. *Phys. Rev. B* **86**, 195141 (2012).
27. de' Medici, L., Giovannetti, G., and Capone, M. Selective Mott Physics as a Key to Iron Superconductors. *Phys. Rev. Lett.* **112**, 177001 (2014).

28. Yu, R., Goswami, P., Si, Q., Nikolic, P., and Zhu, J.-X. Superconductivity at the border of electron localization and itinerancy. *Nat. Comm.* **4**, 2783 (2013).
29. Liu, T. J. *et al.* Charge-carrier localization induced by excess Fe in the superconductor $\text{Fe}_{1+y}\text{Te}_{1-x}\text{Se}_x$. *Phys. Rev. B* **80**, 174509 (2009).
30. Nekrasov, I. A. and Sadovskii, M. V. Electroni Structure, Topological Phase Transitions and Superconductivity in $(\text{K}, \text{Cs})_x\text{Fe}_2\text{Se}_2$. *JETP Lett.* **93**, 166-169 (2011).

Acknowledgements ARPES experiments were performed at the Stanford Synchrotron Radiation Lightsource and the Advanced Light Source, which are both operated by the Office of Basic Energy Sciences, U.S. Department of Energy. The Stanford work is supported by the US DOE, Office of Basic Energy Science, Division of Materials Science and Engineering, under award number DE-AC02-76SF00515. The work at Rice is supported by NSF Grant DMR-1309531 and the Robert A. Welch Foundation Grant No. C-1411. The work at Renmin University is supported by the National Science Foundation of China Grant number 11374361, and the Fundamental Research Funds for the Central Universities and the Research Funds of Remnin University of China. The work at Tulane is supported by the NSF under grant DMR-1205469. The work at Los Alamos is supported by the U.S. DOE Office of Basic Energy Sciences.

Author Information The authors declare no competing financial interests. Correspondence and request for materials should be addressed to D. H. Lu (dhlu@slac.stanford.edu) and Z.-X. Shen (zxshen@stanford.edu).

Fig. 1: Low temperature band structure of iron chalcogenides in comparison to iron pnictide.

Fermi surfaces measured on (a) $\text{FeTe}_{0.56}\text{Se}_{0.44}$ (FTS), (b) $\text{K}_{0.76}\text{Fe}_{1.72}\text{Se}_2$ (KFS), (c) monolayer FeSe film on SrTiO_3 (FS/STO), and (d) $\text{Ba}(\text{Fe}_{0.93}\text{Co}_{0.07})_2\text{As}_2$ (BFCA), shown in BZ notation corresponding to 2-Fe unit cell (For comparison purposes, we use the M point to denote the BZ corner where the electron pockets live for all compounds and LDA, even though for 122 crystal structures, this is the X point), with schematic outlines shown in red. (e) Spectral image of FTS along the Γ -M high symmetry direction, taken with 22eV (26eV) photons for near the Γ (M) point. Measurements along the same cut for (f) KFS, (g) FS/STO, and (h) BFCA, with photon energies of 26eV, 22eV, and 47.5eV, respectively. In-plane polarization was odd with respect to the cut for all measurements, (e)-(g) has additional out-of-plane polarization. (i)-(l) Second energy derivatives for the spectral images above. Observable bands are marked with dominant orbital character (red: d_{xz} , green: d_{yz} , blue: d_{xy}). (m) LDA calculations for KFS³⁰. (n) Schematic based on (m) with d_{xy} orbital strongly renormalized. (o) Schematic based on (m) by introducing hybridization between d_{xy} band and d_{xz} electron band. (p) High resolution spectra of FS/STO showing the presence of two electron bands around M. (q) Γ -M high symmetry cut of FS/STO taken in the second BZ, where d_{xy} orbital matrix elements are strong. The d_{xy} hole band has a lower band top at Γ than d_{xz}/d_{yz} , hence it crosses and hybridizes with the d_{xz}/d_{yz} hole bands, resulting in the apparent sharper curvature near Γ .

Fig. 2: Temperature dependence of the band structure of iron chalcogenides

(a)-(c) Second energy derivatives of band structure along the Γ -M cut of FTS, KFS, and FS/STO, same as that of Fig. 1(e)-(g), taken in the low temperature state at 15K, 10K, 9K, respectively.

(d)-(f) Same as that of (a)-(c) but taken in the high temperature state at 120K, 210K, and 190K, respectively. (g) Schematic showing the band structure in the low temperature state with finite spectral weight of d_{xy} orbital, same as Fig. 1k. (h) Schematic showing the band structure in the high temperature state after d_{xy} orbital completely loses spectral weight.

Fig. 3: Quantitative analysis of temperature evolution in the iron chalcogenides

(a)-(c) Raw spectral images of FTS, KFS, and FS/STO taken in the low temperature state. Yellow regions mark the momentum ranges integrated for energy distribution curve (EDC) analysis for each compound. (d) Integrated EDCs in the yellow region of (a) for FTS at selected temperatures, fitted by a Shirley background (gray), a Gaussian for the d_{xy} band (blue), and a Gaussian for the d_{yz} band (green), convolved by the Fermi-Dirac function. (e) Integrated EDCs in the yellow region of (b) for KFS at selected temperatures, fitted by a Gaussian background (gray), and a Gaussian for the d_{xy} band (blue). (f) Integrated EDCs in the yellow region of (c) for FS/STO at selected temperatures, with a Gaussian background (gray), a Gaussian for the d_{xy} band (blue), and a Gaussian for the d_{yz} band (green). Residual spectral weight for the d_{xy} peak is shaded for each temperature for all compounds. Fitted peaks for the lowest temperature is shown for each compound. (g)-(i) Temperature dependence of the fitted areas of the d_{xy} and d_{yz} peaks for FTS, KFS, and FS/STO. Guides to eye are drawn in gray to show the trends. All curves are normalized by the initial value of the peak area.

Fig. 4: Calculated phase diagram of the OSMP as a function of temperature, U, and electron filling

Slave-spin mean-field phase diagrams of the five-orbital Hubbard model at systematic electron fillings from $n=6$ to 6.15. See Methods for calculation details. Blue shading shows the d_{xy} quasiparticle spectral weight, Z_{xy} . The OSMP phase boundary is shown where Z_{xy} drops to zero. A Mott Insulator (MI) phase exists for $n=6$, where all orbitals have zero spectral weight. The U for FTS, FS/STO, and KFS are estimated from the temperature at which Z_{xy} is observed to vanish, and are shown by yellow strips, while Hund's J is fixed at 0.6eV.

Figure 1

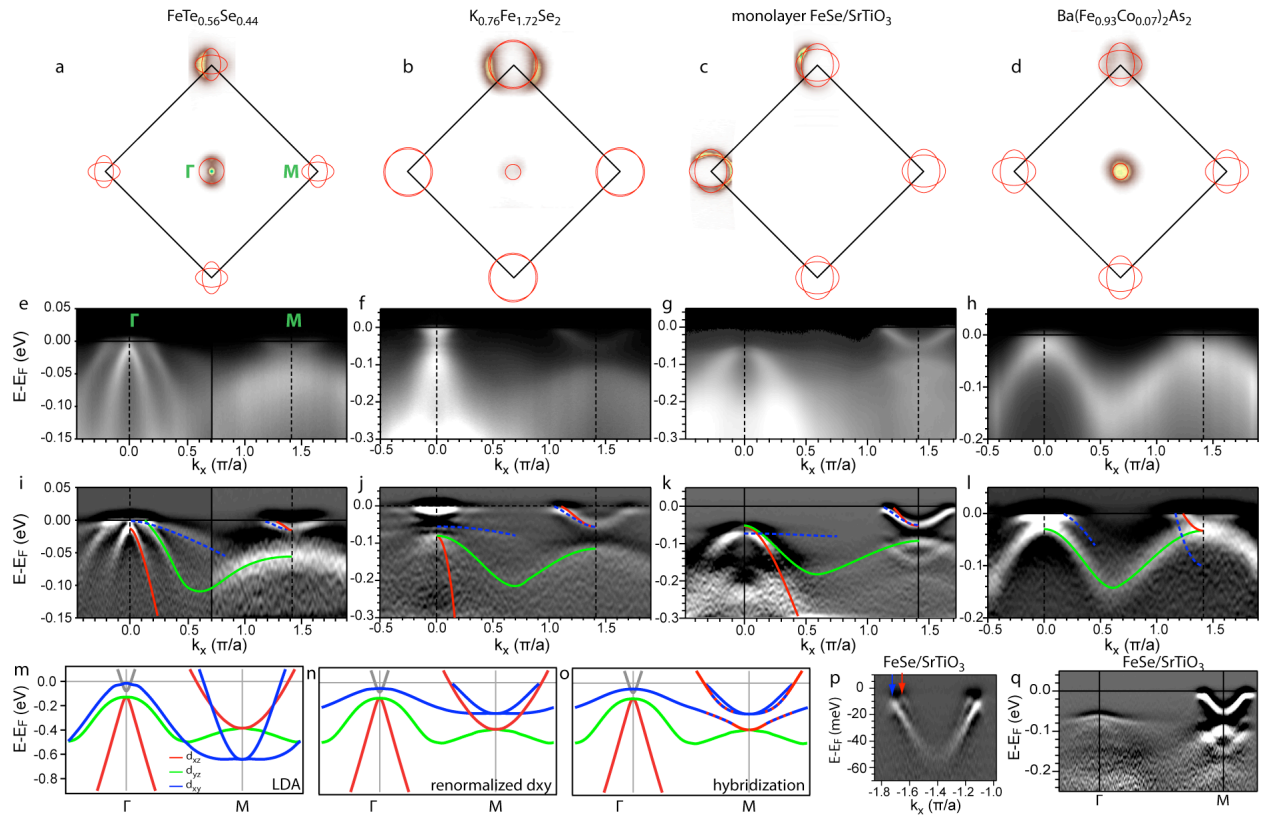


Figure 2

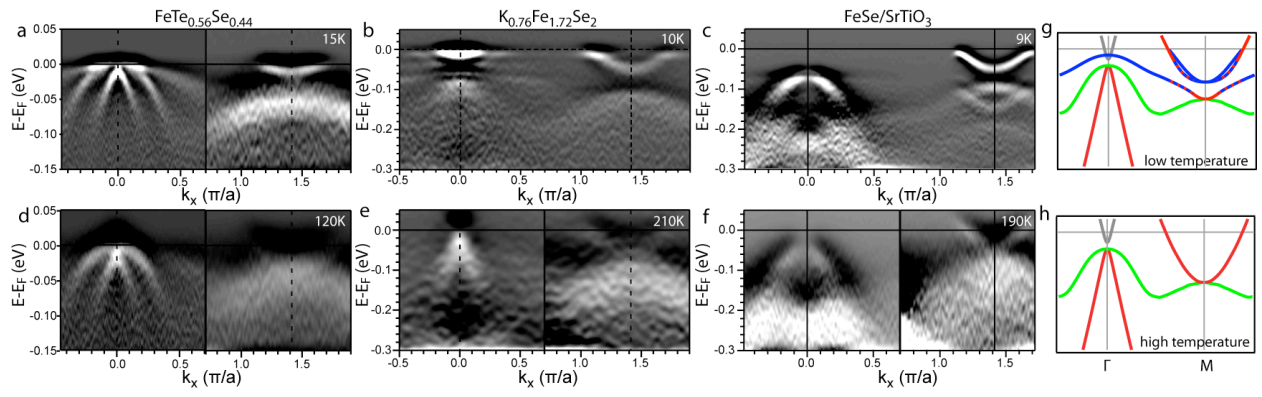


Figure 3

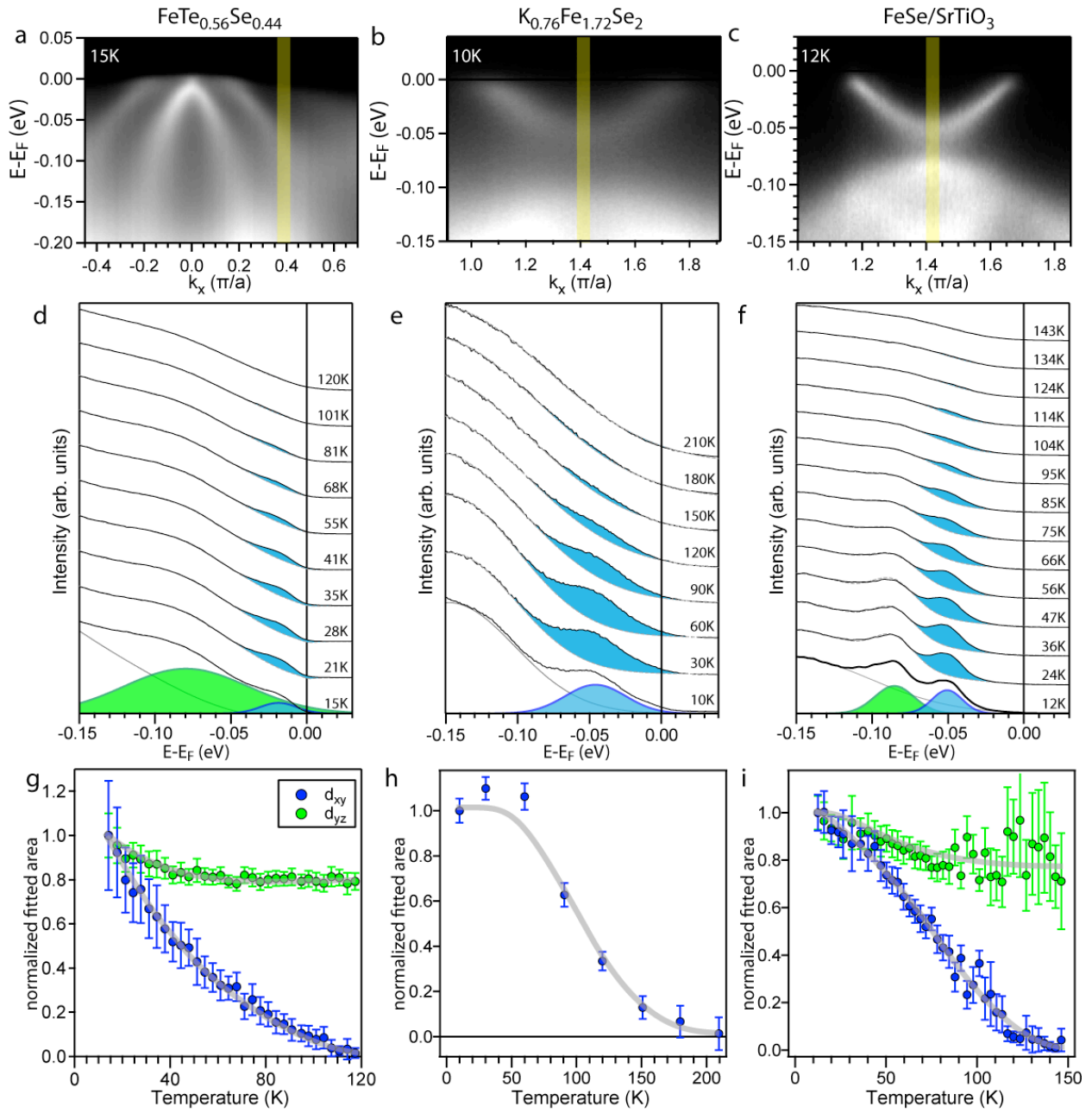


Figure 4

